California State University – Maritime Academy Wind Team

2024 Collegiate Wind Competition
Final Turbine Design Report

Faculty Advisor *– Dr. Thomas Nordenholz | TNordenholz@csum.edu*

Project Manager *– Jasen Nicolas | JNicolas56@csum.edu*
Connection Creation Lead *– Vonne Ng-Bader | Vng-Bader63@csum.edu*
Project Development Lead *– Matthew Rizzi | MRizzi49@csum.edu*

Blades *– Victor Mashevsky*
Mechanical *– Tobias Afdahl & Lucas Kennedy*
Generator *– Nathan Witte & Dayton Huffaker*
Foundation *– Vonne Ng-Bader & Kent Suzuki*
Instrumentation & Electronics *– Nathan Witte, Cyrus Khaleeli, & Jasen Nicolas*

A Very Special Thanks To:

Dr. Tom Oppenheim | Mr. Steffan Long | Mr. Michael Kazek | Mr. Michael Strange | Mr. David Grover
Ms. Samantha Koekemoer | Mr. Guy Sanchez | Dr. Zachary Nosker | Mr. Tom Clyatt | Mr. Josh Short

Many Thanks To Our Sponsors:

Table of Contents

Executive Summary

Cal Maritime's turbine design is a three-bladed, controllable pitch, horizontal-axis turbine fixed to a custom-built radial flux generator. AC power from the generator is rectified to DC power, through a 3-phase full-bridge passive rectifier and is connected to our variable resistive load. Our turbine structure will be supported and anchored into sand by a bucket-type foundation.

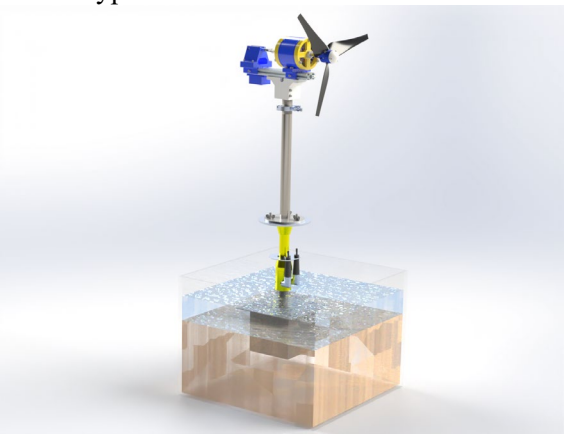

Figure 1: Full Design Render

Our primary objective in the 2024 Collegiate Wind Competition was to create a simple and robust design to maximize effectiveness at completing competition tasks while complying with design constraints. To achieve this objective, we maximize power at wind speeds from 5 to 11 m/s, maintain our rated power and rotor speed at wind speeds from 12 to 14 m/s, conduct shutdown and restart scenarios, and withstand wind speeds up to 22 m/s.

For blades, the airfoil we chose is the A18 which is thinner than the airfoils used by previous years, to maximize aerodynamic efficiency. To offset our thinner design, we manufactured our blades out CF-PLA which is more rigid than materials used in previous years. To further maximize power, we built a custom radial flux permanent magnet generator to eliminate cogging, and a variable resistive load to reach maximum power at wind speeds from 5 to 11 m/s through a perturb and observe maximum power point tracking (MPPT) algorithm.

We developed a new type of controllable pitch mechanism which is used to pitch the blades in safety shutdown and restart scenarios as well as being used in conjunction with the variable load system to modulate power and RPM at wind speeds above 11 m/s. Our pitch system design uses a concentric shaft, with a scotch-yoke mechanism to pitch the blades.

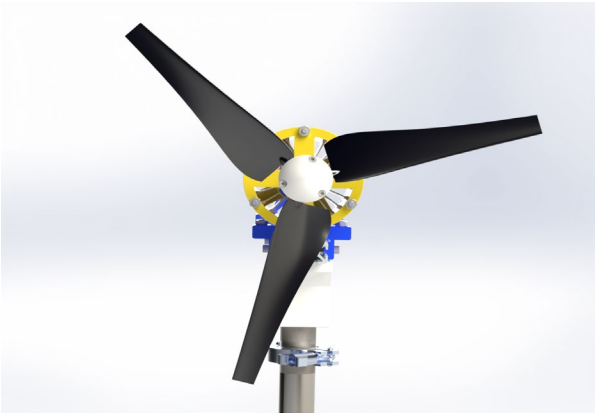

Figure 2: Full Render Front View

To maintain simplicity and ensure proper functionality of the system throughout the entire testing period, a single microcontroller is used on the load side. The system collects measurements from our RPM, windspeed, voltage, and current sensors, and outputs signals to the load and the linear actuator.

Finally, similar to our 2023 counterparts, we ensured that the blades, mechanical systems, and the foundation were properly sized to withstand the loads of the following operating conditions. The first state considered is maximum power at 11 m/s, just before the rotor pitches to shed power. We expect the maximum thrust from the blades in this scenario. The second state is runaway, which captures forces at 14 m/s and 4500 RPM just before we feather our blades. This state will primarily affect the blades as they endure extreme bending moments and radial forces. This shaft speed was determined by disconnecting the load at 14 m/s. The final state under consideration is the durability state, where the wind speed is at 22 m/s and our turbine is below 300 RPM. In this scenario, the maximum aerodynamic drag and maximum total force is experienced by the foundation.

Chapter 1: Turbine Design

1.1 Blades

1.1.1 Airfoil Selection

The focus for blade design this year was maximizing aerodynamic efficiency given the low Reynolds number flow. A thin airfoil would be ideal for this purpose, but airfoils that are too thin quickly approach material stiffness limitations. After iterative testing, the final airfoil chosen was the Archer A18 with a thickness to chord ratio of 7.3% and a peak glide ratio (C_L/C_D) of 48.6 at our expected Reynolds number of 60,000. The A18

airfoil has sharp peaks in its C_L/C_D vs angle of attack (AoA) graph. Although this behavior is undesirable, our rotor maintains a relatively broad power curve, which lends itself to smooth controllability, with near maximum power between a tip speed ratio (TSR) of 3.8 and a TSR of 5, as shown in Figure 3, which corresponds to 1800 to 2500 RPM. Overall, we decided that the trade-off was worth it for better efficiency.

1.1.2 Optimized Blade Geometry

Unlike previous Cal Maritime teams, we used the A18 airfoil along the entire span of the blades instead of blending in a thicker airfoil near the root because research indicates that using multiple airfoils of different thicknesses on a single blade disrupts the smooth transition of flow, increasing drag [5]. Additionally, the blades have a high factor of safety despite the thinner airfoil, as shown in section 1.1.5. The blade geometry optimization and simulation were conducted using Qblade CE version 2.0.6.4. To maximize power, we used the Schmitz optimization method–which is derived from Blade Element Momentum (BEM) theory–to create an optimal chord (c) and twist (θ) distribution. Schmitz optimization requires a design TSR, so a TSR of 4.2 was chosen; both because iterative testing in Qblade showed that it was optimal, and because it is backed by empirical research findings [6]. Since Reynolds number can vary over the span of the blade, from about 40,000 at the root to 60,000 at the tip for the rated wind speed, and because the optimal angle of attack shifts with Reynolds number, the multi-polar blade design function was used, which automatically adjusts the AoA of each section in accordance with the local Reynolds number [1].

1.1.3 Static Performance Analysis

The overall rotor performance was quantified using Qblade, which we used to calculate the non-dimensional coefficient of power (C_P). This was the metric used to compare blade geometries in the design phase. Our final design achieved a max C_p of 0.4. The static performance graph shown in Figure 3 correlates well with real world testing.

1.1.4 Manufacturing/Material

To allow easier manipulation of the blade design in CAD, we developed a plugin for Fusion 360 that takes the blade details from Qblade as well as the airfoil shape and creates a smooth solid body that is much easier to work with, allowing us to integrate the blade root into the blade with ease. Like previous years, the blades were FDM 3D printed at 100% infill, which has the benefit of easy manufacturing and rapid prototyping. We noticed that stiffer materials increased performance by reducing blade deflection, so the material we settled on is carbon fiber filled PLA, with 15% micro carbon strands by weight, and a tensile strength of 48 MPa [2]. This material was chosen for its increased rigidity over regular PLA. Rigidity is measured using the flexural modulus, which is 3200MPa for standard PLA compared to 6320MPa for the CF-PLA [2].

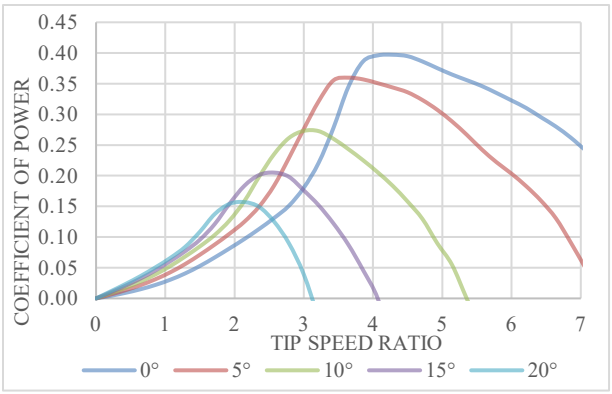

Figure 3: Power Performance Curves

1.1.5 Mechanical Loads Analysis

1.1.5.1 Blade Span

Operating State	Radial Load (N)	Stress (MPa)	Deflection (mm)	Pitching Moment (N-m)	FS
Runaway	270	2.85	0.15	0.06	19
Rated Power	120	1.28	0.09	0.05	43

Table 1: Blade Load Analysis Results

Our mechanical load analysis was conducted using a similar method to the 2023 Cal Maritime team. The wind and radial loads along the span of the blade were modeled as a rotating cantilever beam, with neglected twist. Based on an MIT aerodynamics lecture, we compensated for the area properties of the airfoil-shaped cross section [3]. The blade is subjected to distributed wind loading on the flapwise side, which is calculated by Qblade, and radial loading, which creates stress at the root of the blade and creates a restoring moment that helps the blade resist deflection in an effect known as centrifugal stiffening. To model the deflection of the blades accounting for centrifugal stiffening, we used an iterative solver developed in MATLAB by the 2023 Cal Maritime team, which accounts for centrifugal stiffening with a fourth order differential equation in terms of the centrifugal force, distributed wind

loading, and internal forces as a function of radius [4]. The calculation was done at the rated power state at 11 m/s and 2300 RPM as well as a worst-case runaway state at 14 m/s and 4500 RPM, which occurs momentarily if the load is disconnected at 14 m/s before the blades pitch back. The results of the analysis are compiled in Table 1.

1.1.5.2 Root Connection

To integrate the blade root connection tightly with the mechanical pitch system and maximize swept area for the blades, we redesigned the blade root compared to our Phase II design. The new design consists of a threaded heat set insert mounted directly to the root of the blade, as well as an indexing tab which interfaces with the pitch system to fix the angle of the blade, see Figure 10 for detail. Because the interaction of the heat set inserts and the base plastic is difficult to model, we decided to verify the integrity of the root via direct experimentation. As shown in Table 1, the maximum load we expect the root to be subjected to is 270 N or 60 lbf. We attached a section of blade to a static load testing jig and loaded it with 180 lbs of weights, as shown in Figure 4. The root held up perfectly, which gives us a factor of safety of at least 3 for the blade root. Note that maximum stress occurs at the root of blade, so that is the connection we tested. The ability of the root connection to withstand the expected pitching moment was also tested by connecting the blades to a mock hub and applying load with a force meter at a known moment arm. The root did not deflect when 10x the expected moment was applied.

Figure 4: Blade Root Test

1.2 Mechanical Design

Our design goals with pitch control are to have a robust system with 90˚ of blade rotation. The system is used for the safety tasks to stop the turbine and to regulate the turbine's speed and power during the control power and RPM task.

1.2.1 Pitch Overview

The pitching mechanism we chose is inspired by a controllable pitch propeller used on some ships to control the speed of the vessel. Our miniaturized system is made up of two main subassemblies: the hub in the front, and the actuation linkage in the rear of the turbine, as shown in Figure 5.

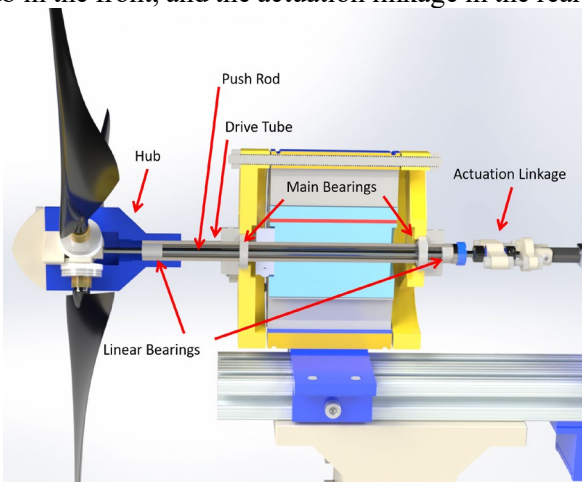

Figure 5: Pitch Mechanism Overview

The generator's main shaft is the drive tube, supported by the main bearings at either end of the generator. This allows us to run a pushrod through the center of the generator, supported by linear bearings on the ends of the drive tube. On the rear of the generator, this pushrod is attached to the actuator linkage, and allows the actuator to move the pushrod, rotating the blades. This movement is provided by the Actuonix L12-30 linear actuator. In the hub on the left side of Figure 5, the pushrod is connected to the control crosshead, which is a triangular shaped block with a transverse groove at its midpoint, as shown in Figure 6. The crosshead is the translating link of the scotch yoke mechanism, which when translated linearly causes the blades to rotate. Each of the three blades is mounted to a blade controller that holds the blade into the hub. The blade controller is made up of a disc, pin, and a post as shown in Figure 10. The pin is located at the edge of the disc, and rides in the groove of the crosshead with a tight tolerance. As the crosshead moves, the blade controller is rotated by the action of the pin-groove arrangement, as seen in Figure 7. Subsequently, the blade controller posts and blades are rotated in a collective fashion.

1.2.2 Pitch Assembly

The hub shown in Figure 6 is made up of two casings which serve as the structure for the scotch yoke mechanism. Each of these casings have three semicircular indents which fit the blade controllers and provide support surfaces. Each blade and blade controller set is provided with a PTFE sleeve bearing to reduce friction. Each blade controller also has a needle thrust bearing, which allows it to rotate freely

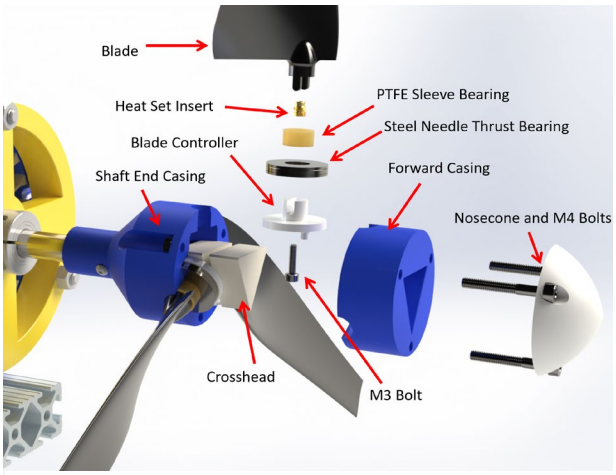

Figure 7: Turbine Hub Exploded View

while absorbing the centrifugal load from the blades. The crosshead is housed in the center and its corners interact with the casing so that the drive tube and push rod rotate together. The hub casings and crosshead are made of 3D printed PETG which is strong and has low surface friction. We chose to machine the blade controllers out of acetal Delrin for its high strength and low friction.

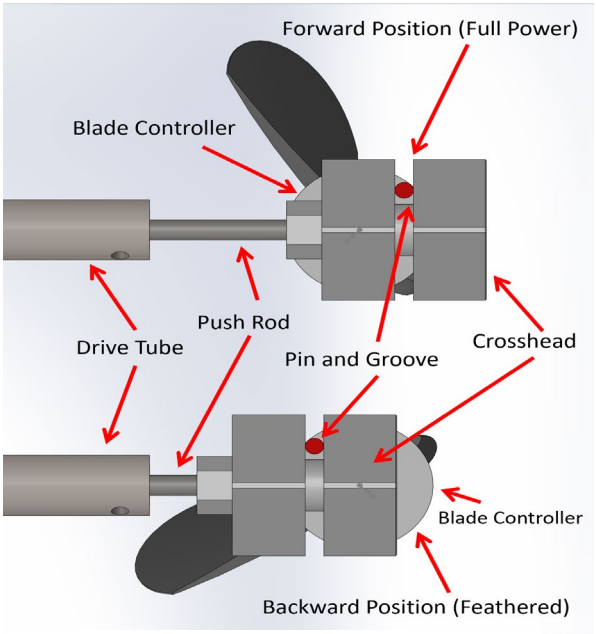

Figure 8: Hub Motion Diagram

The system is set up so that the forward position of the crosshead sets the blades in their full power position, and pulling backward feathers the blades. While the blades are in the full power position, the controller pin angle θ is 45˚ forward relative to the plane of blade rotation. The controller and pin can rotate back to -45˚ to feather the blades. This arrangement allows for a 90˚ range of motion and

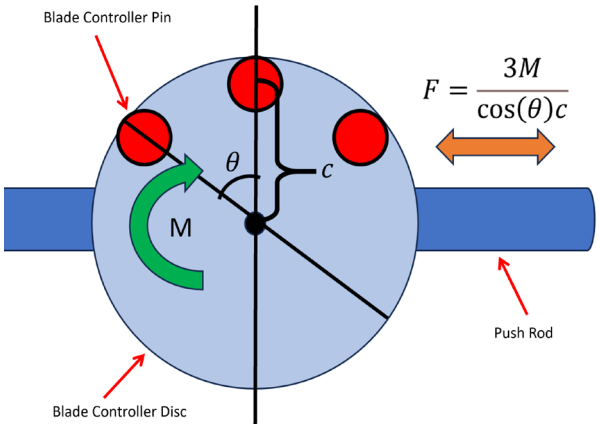

Figure 6: Blade Controller Analysis

reduces the chance that the pin binds up the system by getting stuck. Using the applied moment (M) of the blades from Table 1 of 0.06 Nm at rated speed, we calculated the force (F) against the push rod to be 23.3 N (See Figure 8). This prompted us to select the Actuonix L12 actuator with a 210:1 gear ratio, which has a maximum force output of 80 N and a back drive force of 45 N [10]. Additionally, based on the geometry and the resolution of the L12 of 0.2 mm, we estimate the system to have 1.05˚ of angle control resolution of the blades.

1.2.3 Actuation Linkage

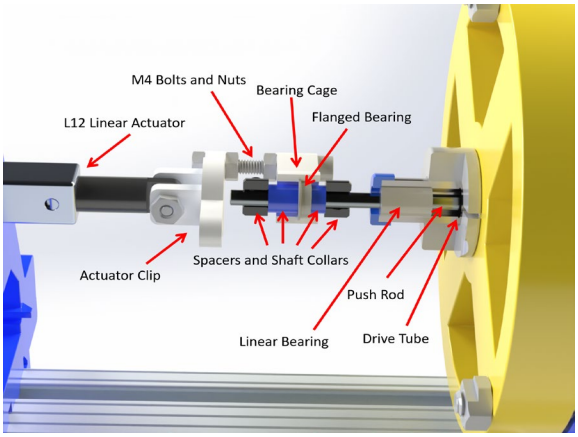

Figure 9: Actuation Linkage

The linear actuator at the back of the turbine controls the motion of the crosshead. The crosshead and actuator are connected by a pushrod which runs through the generator and to the linkage. The pushrod linkage consists of a flanged bearing, seated within a bearing cage. The bearing cage is bolted to the linear actuator. Movements from the actuator are transferred through the bearing cage to the outer race of the bearing. The inner race of the bearing is provided with spacers and shaft collars on either side

to transfer the movement to the pushrod, and subsequently the crosshead in the hub.

1.2.4 Blade Connection

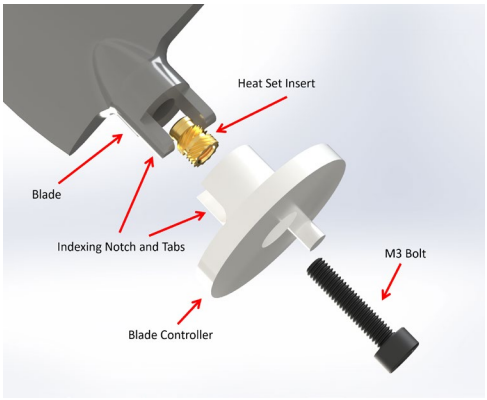

Figure 10: Blade Root Connection

The blade root connection needs to securely mount the blade and index it correctly so we can have accurate control of the blade angle, as shown in Figure 10. This was accomplished by creating a notch and tabs in the blade and blade controller, respectively. The blade controller has a counterbored hole in the bottom, through which an M3 bolt is inserted and screwed into the heat set insert at the bottom of the blade. The counterbore allows the blade controller to still have a flat surface which rides on the crosshead.

1.2.5 Stress Calculations

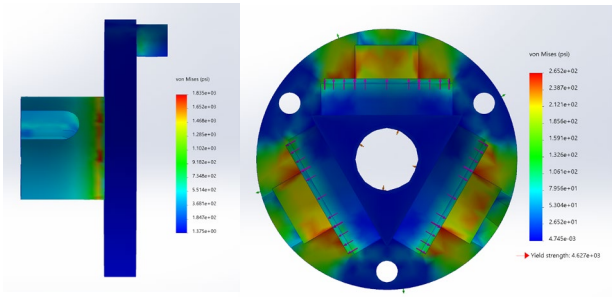

Figure 11: Axial Load on Blade Controller and Hub Casing Radial Loading

The part that brought up the most concern with loading in this design was the blade controller. It is subjected both to the axial load from the centrifugal force of the blades as the rotor spins, as well as the moment exerted by the blades on their axis. The blade controller must withstand both of these forces to keep the blade held in its position in the casing and hold its angle relative to the shaft. Referring to Table 1, the centrifugal force of the blade in the runaway state is 270 N, or about 60 lbf. This causes the highest stress we see in the form of an axial load concentrated at the base of the blade controller's post, as seen in Figure 11. The maximum stress is 1840 psi and the acetal Delrin has a yield strength of 9500 psi [7], giving a safety factor of 5. Additionally, the moment from the blades is being exerted onto the pin of the blade controller. From Table 1, the moment of 0.06 Nm from the blades induces a maximum stress of 734.9 psi, so the pin of the blade controller has a safety factor of 13. The hub casings also experience the same 270 N (60 lbf) in each of the three blade controller indents. The maximum stress induced is 265 psi which is dwarfed by PETG's yield strength of 4,627 psi [9]. The casings have a safety factor of 17.

1.2.6 Nacelle and Tower Assembly

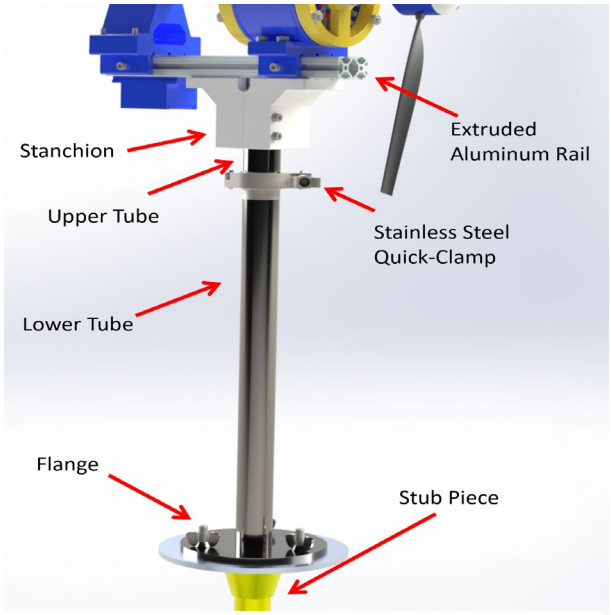

Figure 12: Nacelle and Tower Assembly

As shown in Figure 12, the nacelle features our blades, pitch system, generator, mounting rail, stanchion, and upper tube. The blade and pitch system are secured to the generator and linear actuator assembly, which are both fastened to an extruded aluminum rail, allowing for ease of installation and modularity to the design. A stanchion, adjustable along the bottom length of the rail, secures the upper tube by compressing around it using two bolts and nuts. The upper tube features a male fitting, located just below the stanchion.

Also shown in Figure 12, the tower features the lower tube with a female fitting at the top and a flange at the bottom, attaching the entire assembly to the competition-provided stub piece. The male and female fittings are secured using a quick-clamp,

enabling us to quickly install and remove the nacelle and/or tower without interfering with the foundation. The stanchion and the quick-clamp allow us to easily yaw the nacelle to align the turbine with the wind direction.

1.3 Foundation

In the past two years, we used a quadpod design but during last year's competition, one of the legs sheared off due to a weld failure. To address this issue, we created a bucket-type design that distributes forces over a larger surface area, rather than concentrating loads. It utilizes compression and friction forces to keep the structure in place, while maximizing use of the overall volume.

Figure 14: Bucket Foundation Prototype

1.3.1 Foundation Integrity Analysis

1.3.1.1 Turbine Expected Loads

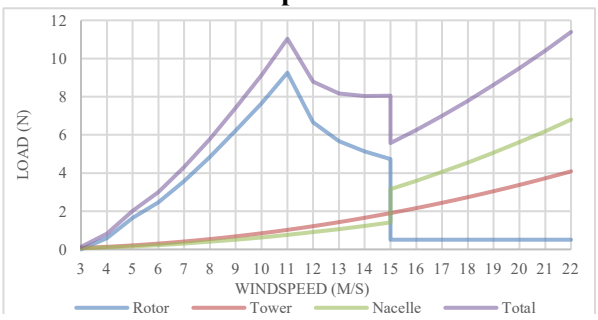

Figure 15: Expected Turbine Loads with Pitch

As seen in Figure 14, the main sources of load being applied to the turbine are thrust from the rotor and drag from the tower and nacelle. The data for the thrust generated by the rotor is derived from a QBlade simulation. Once the wind speed exceeds 11 m/s, the thrust force of the rotor decreases due to the feathering of the blades. After 15 m/s, the thrust from the blades drops due to feathering, but the load on the nacelle increases due to the loss of the axial induction factor from the rotor. For the tower and nacelle drag calculations, the tower was modeled as a vertical cylinder, and the nacelle was assumed to have a high drag coefficient of 1.4 due to its complex geometry. These assumptions give a conservative estimate of drag. To increase our confidence, we also simulated the expected loads if the blades fail to pitch, shown in Figure 15. For this situation, the load that's being applied on the rotor continues to

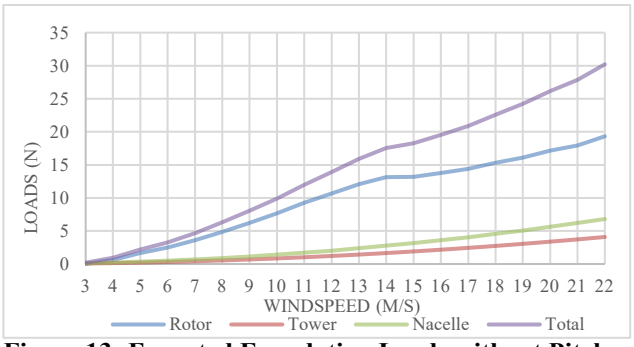

Figure 13: Expected Foundation Loads without Pitch

increase as wind speed increases. For this worst-case scenario, the expected load is 30 N at 22 m/s.

1.3.1.2 Free Body Diagram

Every component of the turbine induces an overturning moment on the foundation. When the force from the nacelle, tower, and rotor is being applied, the foundation overcomes the moment by utilizing a combination of soil interactions as shown in Figure 16. The sand is compacted by the top plate adding to the compression forces on the side walls. Inside the bucket the weight of the sand acts as a deadweight holding the foundation in place. With a combination of these factors, the foundation can be secured in the sand with minimal horizontal displacement.

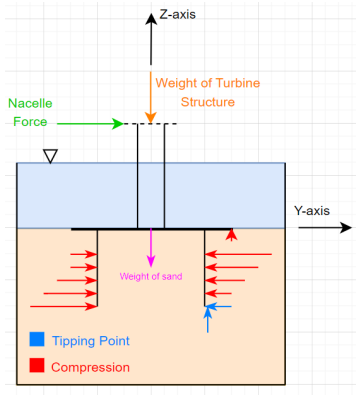

Figure 16: Foundation Free-Body Diagram

1.3.2 Manufacturing Process

The foundation was manufactured by laser cutting and bending sheet metal into a square shape to create the side walls. After bending, seams of two side walls were TIG welded. Since the weld was on a wall face, there is no concern of the weld failing. Shown in Figure 17, the side walls have a width of 20.32 cm (W_S) and depth of 16.51 cm (D), and the dimensions are the same for all sides. The top plate was then laser cut and welded on the top of the side walls. The top plate has dimensions of 25.4 cm by 25.4 cm (W_T). All dimensions are in accordance with the competition rules.

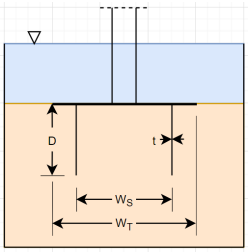

Figure 17: Side Profile of Bucket Foundation

1.3.3 Durability/Load Testing

To simulate the expected loads on the foundation, we used a force meter as a substitute for the drag forces. After placing the foundation into the test area, we inserted a 95 cm tall connection piece to simulate where the turbine drag forces will be applied. To simulate the "failed displacement" condition, we placed a piece of tape 25 mm away from the foundation piece, as shown in Figure 18. Next, we pull on the connection piece with the force gage from the appropriate height to simulate all the forces on the turbine. Once the foundation touches the tape, we make note of how much load it could withstand before displacing. By doing multiple tests, we can get an accurate idea of what load the foundation can consistently withstand and can guarantee that it will hold up to repeated installations.

Figure 18: Foundation Load Testing

1.3.4 Foundation Design Iterations

Multiple iterations of the foundation design were manufactured, varying the thickness of the side walls and the top plate. The experimental data in Table 2 showed that thinner wall designs could withstand less load. The decision had to be made whether we prioritize structure weight over durability, and we decided that the durability and the load it could withstand will take precedence, in order to ensure a passing score for the Durability Task.

Comparing the nacelle load data in Figure 14 to the collected data in Table 2, the maximum expected load of 14 N is dwarfed by the observed capability of 62 N for the 0.075" design. The factor of safety of 4 meets our goal of ensuring a passing score for the durability task. It even covers the maximum expected load in the worst-case scenario where the blades don't pitch back at all, shown in Figure 15, with a factor of safety of 2.1.

Table 2 Foundation Test Results

Wall Thickness	Trial 1	Trial 2	Trial 3	Trial 4	Average
0.060"	53 N	53.5 N	44.5 N	44.5 N	47.7 N
0.075"	35 N	50 N	67 N	63 N	62 N

To determine how much the sand in the bucket affects foundation performance, a test was conducted which consisted of digging a hole in the tank of sand, placing the foundation in the hole, packing the outer walls with sand, then measuring the force required to displace the foundation. This was to measure how much the compression forces, shown in Figure 16 contribute to the overall durability. The results shown in Table 3 suggest that the force the sand is applying onto the inner walls contributes to half of the total load it would otherwise withstand.

Table 3 Foundation Test Results without Sand

Wall Thickness	Trial 1	Trial 2	Trial 3	Trial 4	Average
0.060"	24 N	25 N	28 N	26 N	25.75 N
0.075"	35 N	38 N	41 N	36 N	37.5 N

1.4 Generator

1.4.1 Overview

The generator we decided on is a custom-built three-phase permanent magnet generator. A custom-built generator was chosen because of the team's experience building them for previous projects, to reduce cogging torque compared to off-the-shelf options, and to manipulate power output characteristics. The generator consists of two primary parts: the stator and the rotor. Each part was designed using SolidWorks and 3D printed in PLA.

1.4.2 Rotor Design

The rotor has eight magnetic poles, with eight additional smaller magnets oriented perpendicular to the main magnets, creating a Halbach array.

Figure 19 Finished Rotor

The purpose of the Halbach array is to focus the magnetic flux of the main magnets outward towards the coils. This effect was confirmed in the QuickField magnetic flux simulation software, shown in Figure 20. This increase in magnetic flux improves the power for a given rotor without increasing the number of poles. In addition, the use of smaller Halbach magnets also allowed us to fit more magnets on the outer edge of the rotor, further increasing the magnetic flux density.

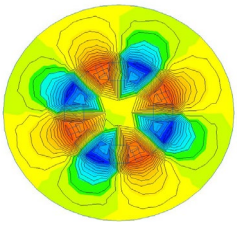

Figure 20: 8-pole Halbach Magnetic

The other focus of the rotor design was the structural integrity of the rotor and the magnets. We found upon analyzing the rotor itself, using SolidWorks

FEA, that the epoxy would be the weakest link. Knowing this we verified that the magnets would be held in by the epoxy. Using rotational kinematics, we found that the stress on the epoxy would not exceed 251 psi, which has a safety factor of 13 with the bond strength of 3300 psi [8].

1.4.3 Stator Design

Table 4 Stator Details

Generator Details	V1	V2	V3
# of Coils	9	24	24
# turns per coil	100	24	18
AWG	22	22	20
Max Power Curve Voltage	26	30	33

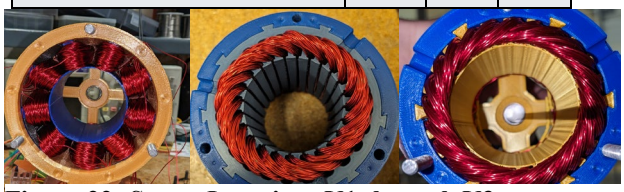

Figure 22: Stator Iterations V1 through V3

When designing the stator, we focused on ease of assembly, and modularity of the stators. This was done so an iterative approach could be used to find the highest-performing stator. The configurations, shown in Figure 21, were designed and built to be tested and compared. V1 (left) was built with 9 concentrated windings and was based on generators we have seen from previous Cal Maritime teams. V2 (middle) and V3 (right) both used distributed windings which allows for tighter packing of coils. All generators are wired in Delta, because in Wye, the voltages exceeded 48 V. Wiring in Delta reduces voltage of the generator by a factor of $\sqrt{3}$.

1.4.4 Operating Voltage/Performance Testing

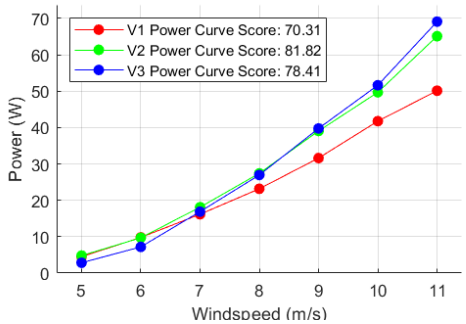

Figure 23: Generator Comparison Power Curve

All three stators were tested in a mock power curve test. The tests were conducted sequentially with all other equipment and conditions remaining the same. As shown in Figure 22, the V2 stator scored the highest, despite not having the highest peak power. V2 also fell in the middle of the pack for voltage as shown in Table 4. Due to the higher score and desirable voltage at peak power, the V2 stator was selected.

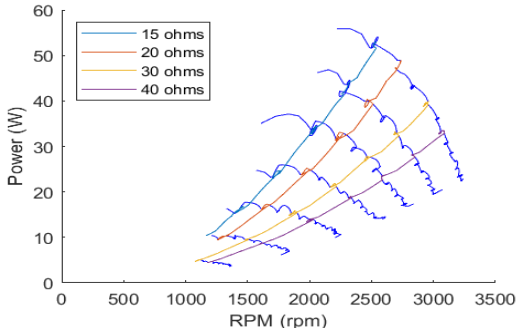

Figure 21: Generator Resistance Sweep

In addition to the power curve testing, we also established a range of optimal resistances shown in Figure 23. This generator model shows the response to certain electrical conditions and informed the electrical system design.

1.5 Electrical and Instrumentation

The electrical system is made up of the generator itself, the turbine box, and the load box. The turbine box includes the rectifier, peripheral instruments, and their necessary power converters. The load box contains our variable resistive load, microcontroller, and backfeed system. Power flows from the generator to the turbine box, through the PCC, and to the load box. Data is communicated via an I2C network that is optically isolated between the turbine and load boxes.

1.5.1 Turbine Side Electronics

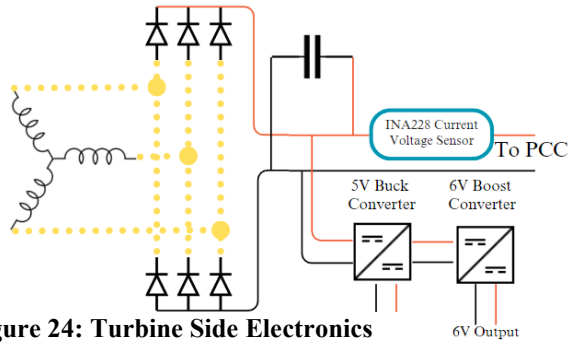

Figure 24: Turbine Side Electronics

The turbine side electronics, shown in Figure 24, link the generator to the PCC. The generator produces 3-phase AC, which we need convert to a stable DC output for the PCC. The off-the-shelf passive 3-phase full bridge rectifier we selected uses six diodes to convert the AC power created in our generator to a DC source. Although the rectifier

outputs DC, it still has ripple from the sinusoidal input, so we include a capacitor on the turbine side high voltage bus to smooth the output to the PCC. Additionally, the capacitor acts as energy storage for the load disconnect task.

All turbine side equipment is powered via a 5 V buck converter for the instrumentation and a 6 V boost converter for the linear actuator. These converters draw power from the turbine side high voltage bus. Typically, this bus is powered by the generator through the rectifier. However, when the generator is not supplying the required voltage to power the turbine side electronics, power is backfed from the load side of the electrical system.

With the current design, voltage stays below the 48 VDC limit due to the generator configuration. To further ensure the voltage limit is not exceeded, we will be implementing a voltage regulating circuit. This circuit uses a comparator op-amp to control two MOSFETs to engage or bypass an off-the-shelf 45 VDC regulator.

1.5.2 Load Side Electronics

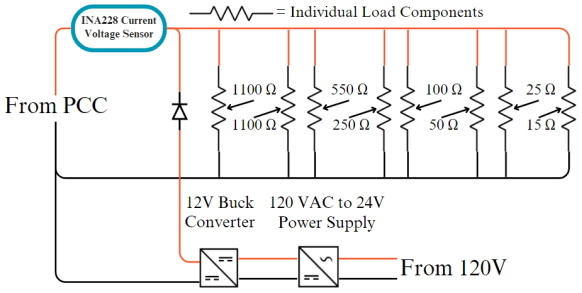

Figure 25: Load Side Electronics

The load side takes the power coming through the PCC and provides the load where the power is dissipated. To achieve maximum power for every given operating condition, we vary the resistance being applied to the generator.

1.5.2.1 Resistive Load

Our variable resistive load design mimics a parallel decade box. The nine individual load components contain different power resistors, each in series with an N-type MOSFET, as shown in Figure 26. Each individual load component is controlled by a microcontroller pin, and they are placed in parallel with each other, as shown in Figure 25.

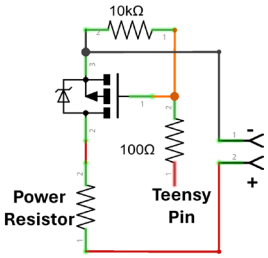

Figure 26: Individual Load Component

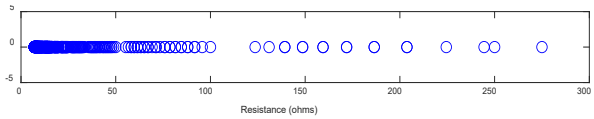

Figure 27: All Possible Load Resistances

Figure 27 shows how switching different power resistors on and off with their respective MOSFETs allows a wide range of resistances to be created. We use logic level MOSFETs, meaning they can be easily driven directly by the 3.3 V digital pins of the Teensy 4.1. This working design is incredibly reliable and has been used for all turbine tests to ensure reliability.

1.5.2.2 Backfeed

Additionally, we use the wall power on the load side to provide a stable power source to the turbine side when it loses power. 120 VAC wall power is converted to 24 VDC, for the load side fans, and is then stepped down to 12 VDC for the backfeed, shown in Figure 25. This power is then passed through a standard diode and into the positive side of our load side high voltage bus. The use of a diode allows for passive transfer from wall-supplied power to generator-supplied power, keeping our turbine side of the system online in all conditions except an extended load disconnect.

1.5.3 Instrumentation

Measuring operating conditions of the system is the primary basis of control for the entire turbine. The instrumentation system includes various sensors to collect data. Using this data, the software will determine how to use the controllable outputs to change the turbine operating conditions.

1.5.3.1 Turbine Instrumentation

The turbine has three devices mounted locally: sensors to measure RPM and wind speed, and a controllable linear actuator to manipulate the blade angle. The RPM sensor is mounted on the generator casing to detect changes in magnetic flux from the rotor. It is a hall effect sensor that measures the change in polarity of the magnetic field as the rotor spins. A high (5 V) or low (0 V) signal is sensed depending on the polarity of the magnet passing the sensor [11]. Wind speed is measured using a pitot tube and a differential pressure sensor [12]. The local wind speed can be found using the difference of pressures and a basic form of Bernoulli's equation. The linear actuator takes a 0-5 V analog input, which is correlated to a position setpoint that the PID loop seeks to achieve [10].

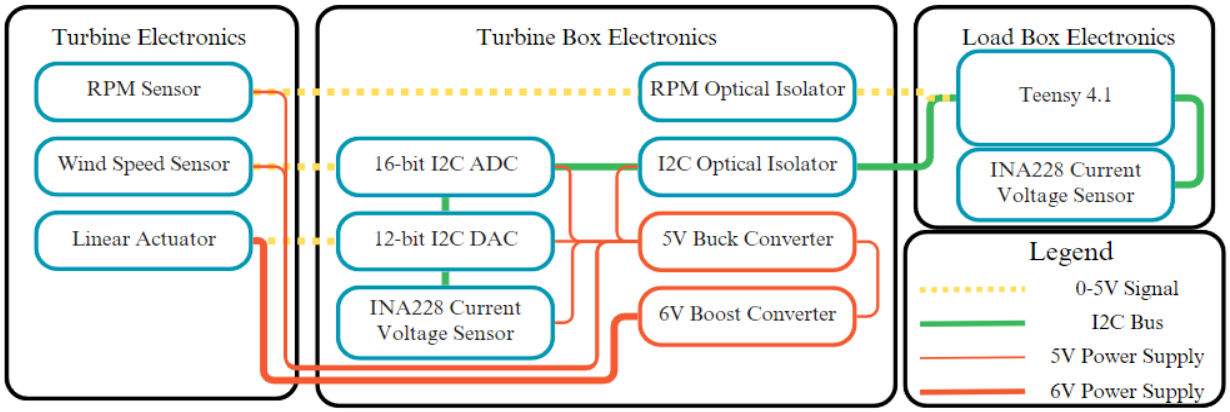

Figure 28: Instrumentation Wiring Diagram

1.5.3.2 Turbine Box Instrumentation

The turbine box includes the instrumentation required to communicate with the turbine instrumentation, measure the power on the turbine side, and send the information to the load box. We use a 16-bit I2C analog to digital converter (ADC) to read the wind speed sensor 0-5 V signal [13]. A 12-bit I2C digital to analog converter (DAC) sends a 0-5 V signal to the linear actuator [14]. Voltage, current, and power are measured via an INA228 20-bit I2C power monitor [15]. All I2C devices are chained together to the optically isolated I2C turbine box to load box connection. Our system has two bidirectional optical isolators, one for passing the digital RPM signal to the microcontroller and the other for the general I2C communication network, which includes the rest of the instrumentation [16]. These optical isolators allow data to be transferred with both sides electrically isolated. This prevents any power flow between the load box and turbine box through the data connections.

1.5.3.3 Load Box Instrumentation

The load box includes the Teensy 4.1 microcontroller and an additional INA228 power monitor. The Teensy 4.1 acts as the brains of the entire turbine and communicates with the turbine side via the optically isolated I2C bus shown in green [17].

1.6 Software

1.6.1 Individual Component Development

After completing a control system design of what sensors and controllable outputs we wanted to incorporate, the software for each component was developed. Many of the components we used, especially the ones from Adafruit, came with pre-written Arduino libraries. These libraries could be used to easily get data from each sensor individually for component verification and testing.

We also developed code for some of our custom components, like our RPM sensor. The RPM sensor, as mentioned in section 1.5.3, is a simple hall effect sensor. We can measure the time it takes for the polarity to switch 10 times, and multiply by a factor related to the number of poles to get the RPM.

Another sensor that required extra work was the wind speed sensor. We chose to calibrate the wind speed sensor against traditional manometers, to ensure the pressure difference measurements were accurate. From here we could implement Bernoulli's equation which transformed the delta pressure measurement to a wind speed measurement.

1.6.1.1 Load Control Code

As described in section 1.5.2.1, we can vary our resistance by switching different MOSFETs on and off. To choose which switches should be open to achieve a desired resistance we used a lookup table generated in MATLAB. The lookup table consists of all possible resistances available, and what combination of switches is needed to achieve it. We can then choose the nearest possible resistance to what we need and activate the necessary MOSFETs to achieve the desired load.

1.6.2 Integration of Components

After developing individual codes for all our instrumentation, we created a library for the entire turbine control system to streamline the program that the microcontroller would be running. The library has functions to pull data from each sensor and manipulate each controllable output. The library uses the work we had done individually on each sensor, but without needing to repeat the code each time, which made implementation into a state machine easier and more readable.

1.6.2.1 Integration Testing

Once the individual code and the electrical wiring was developed, we first wrote code that allowed manual control of the linear actuator and resistance, while recording all the sensor data. This helped us to work out many of the integration bugs before moving on to a system that could control itself through each task.

1.6.3 State Machine

Our final turbine code builds off everything we wrote before and compiles it all into one state machine-based control system. The state machine includes a state for each task in the competition testing, and the transitions determine which state the machine should be in at any set of conditions, as shown in Figure 29.

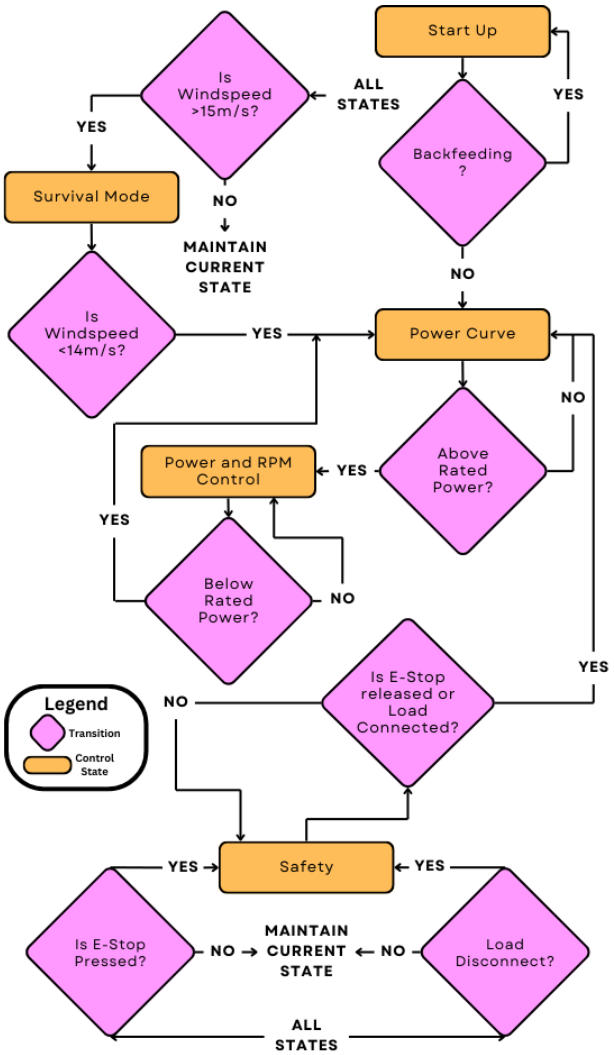

Figure 30: State Machine Flow Chart

1.6.3.1 Start Up

The Start Up state is where the turbine begins testing. The goal of the Start Up state is to improve the cut in speed of the turbine and overcome the backfeed voltage. If the blades are not spinning the pitch is set to a blade angle of 9° which was found in testing to decrease the cut in speed from 3 m/s to 2 m/s. Once the turbine is above 100 RPM the pitch will be set to 0° to maximize the RPM and power. Once the turbine is spinning at 1000 RPM, it will generate more than 12 V which is enough to overcome the backfeed voltage. This will cause the turbine side voltage to increase beyond 12 V, which when measured will make the turbine transition to the Power Curve state.

1.6.3.2 Power Curve State

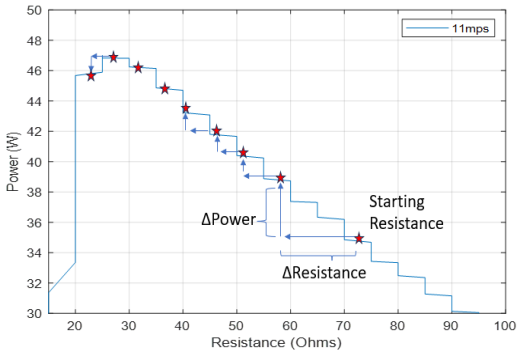

Figure 29: Perturb and Observe Algorithm

The goal of the Power Curve State is to maximize the power by altering the resistance of the load. This is accomplished using a perturb and observe algorithm, which relies on measurement of the change in power to determine the direction of the next change in resistance. Figure 30 contains data we took at various resistances and shows how our algorithm would respond to its starting resistance of 72 ohms. The resistance step size is dependent on the current resistance value, meaning that for higher resistance values the step size will be larger. This is done to decrease the settling time and works well because changes at higher resistances have smaller effects on power and RPM. The direction of each step is determined by whether the power increased or decreased with the last change in resistance. For example, when the resistance passes over the peak of the curve shown in Figure 30, the power will decrease causing the direction of the next resistance step to be positive. These steps are taken every 2.5 seconds, to allow for the turbine to reach a new steady state power, as shown in Figure 31. The Power Curve state is used from when the turbine

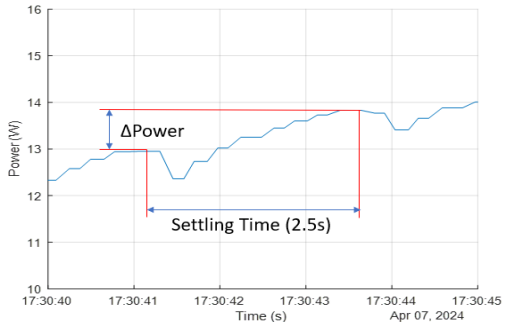

Figure 31: Power Curve Settling Time

transitions out of the Start Up state until the turbine reaches its rated power for more than 10 seconds. Once this occurs the turbine will set the current power and RPM reading as the rated power and transition to the Power and RPM Control state.

1.6.3.3 Power and RPM Control Task.

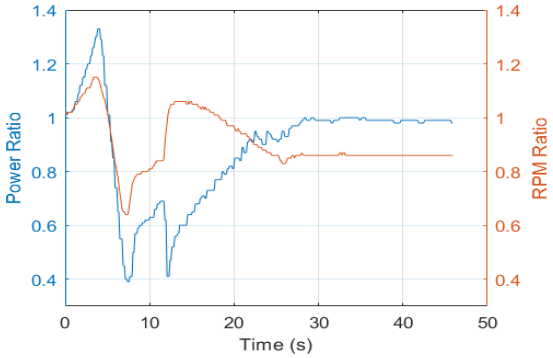

Figure 32: Control Power and RPM Task Test Data

The Power and RPM Control state seeks to maintain the power and RPM that was measured when the state began. To accomplish this, the program has two controllable outputs: pitch and resistance. In testing we found that pitch control is useful for shedding power at higher wind speeds, but with our accuracy capabilities getting fine power control with only pitch was a challenge. For that reason, we use pitch control to reduce the RPM to between -15% and +8% of the rated RPM. Then the resistance control takes over is used to finely adjust the power until it is ±8%. These guidelines help to decrease the settling time by widening the acceptable power and RPM windows, while still ensuring Power and RPM Control Task scores above 48 points. Figure 32 shows data from a test in which the wind speed was increased from 11 m/s to 13 m/s, the settling time was about 20 seconds, and the final score was 50 out of 50.

1.6.3.4 Safety Stop and Load Disconnect

Both the Safety Stop and Load Disconnect Tasks are accomplished by the same Safety state. Any state can transition to the Safety state at any time. This state can be activated by either detecting the E-stop being pressed or detecting a load disconnect. To detect the E-stop being pressed we send one lead to ground and the other to a pulled-up microcontroller pin, which reads whether the pin is high or low. This arrangement is designed for a normally closed E-stop switch. In order to detect a load disconnect, we compare the load and turbine side voltage. If the load side drops to 12 V (which is held by the passive backfeed), while the turbine side stays where it was, a load disconnect is triggered. For the E-stop and load disconnect situations the blades are commanded to feather. Both the E-stop and load disconnect have been tested from 5-15 m/s in our wind tunnel as shown in Figure 33. We feel this is representative of the full operating conditions, as above 15 m/s we plan on having the blades feathered for the survival task.

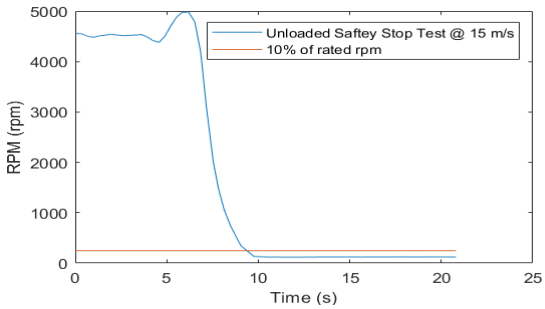

Figure 33: Safety Stop Task Test @ 15 m/s

1.6.3.5 Survival Task

Any state, except the Safety state, can transfer to the Survival state if the wind speed exceeds 15 m/s. At this point in testing, power generation is no longer required. To reduce the rotor thrust, the blades are feathered, reducing the load that is put on the foundation above the cutoff wind speed.

Chapter 2: Full Turbine Assembly

2.1 Full Turbine Integration

Our turbine consists of three main components: the nacelle, the tower, and the foundation. The nacelle features our blades, pitch system, generator, mounting rail, stanchion, and the upper tube with a male fitting at the bottom. The nacelle is secured to the tower via mating the respective fitting and fastening a quick-clamp. The tower assembly, with its flange, mates with the competition provided stub piece with wing nuts. Yaw adjustment is possible at the stanchion and quick-clamp. The stub piece mates with the foundation. Finally, to connect the electrical

system to the turbine, the power and signal wires run through the tower, stub piece, and foundation.

2.2 Distributed Team Environment

This competition is our members' senior capstone project. We delegated our team members into subteams based on interests and previous experience. Our team meets weekly to ensure all subteams are up to date on the progress of the entire turbine and all design changes maintain compatibility with other sub-systems. Each subteam is primarily made of two members with each having one lead. Initially, as a whole team, we decided on bigger design choices such as horizontal axis versus vertical axis, variable or fixed pitch. Then, given these major decisions, each subteam did research on their design. These designs were pitched to the whole team and were chosen based on feasibility and effectiveness at achieving our design objectives. From that point forward each subteam has prototyped their designs while ensuring compatibility with other subteams. As we moved into Phase III of the competition, next year's team began attending our weekly meetings and we have been integrating them into the testing and analysis process to ensure the longevity of the team in future competitions.

Chapter 3: Turbine Testing Results

3.1 Wind Tunnel Testing

With our wind tunnel built from our alumni, we were able to conduct testing up to 14 m/s allowing us to successfully test most competition testing tasks including: Power Curve, Rated Power and Rotor Speed, and Safety Shutdown.

The results of our Power Curve task test can be seen in Figure 34, where we scored a total of 81.82 points. We believe it is highly possible our actual wind speed is higher than our measurements, leading to higher power than might be possible. With this caveat, we were able to determine the rated characteristics of our turbine. Our Rated Power and Rotor Speed are 63.45 W and 2500 RPM.

The results of our Rated Power and Rotor Speed task test can be seen in Figure 35, concluding that we are able to maintain power within a 3% band and rotor speed lower than our rated characteristics. This results in a score of 50 points in this task. Finally, we were able to test the Safety Shutdown Task up to 14 m/s, where we were able to successfully able to shut down and restart in both the E-Stop and Load Disconnect scenarios, netting us full points.

3.2 Field Testing

To ensure that our that our foundation can support the rest of our turbine assembly at wind speeds up to 22 m/s, as previously stated, we performed a conservative theoretical analysis to predict the maximum amount of force experienced by the full turbine and then conducted a pull test. In the worst-case scenario, where our blades do not feather past 15 m/s, our foundation must be able to withstand 30 N. Through our pull tests previously explained, our final foundation design was able to withstand 62 N which resulted in a safety factor of 2.

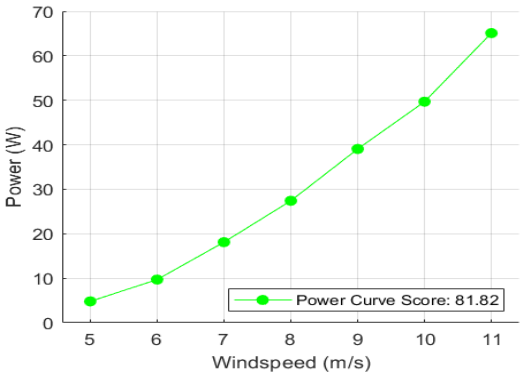

Figure 35: Power Curve Test Data

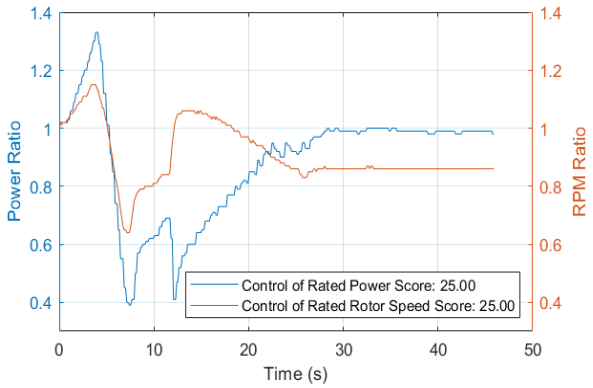

Figure 34: Control Task Test Data

To ensure that the tower assembly and the nacelle are also able to withstand wind speeds up to 22 m/s we are developing a mount that is able to secure the turbine to a truck bed. Additionally, through this test setup we will be able to verify safety shutdown and restart procedures at wind speeds higher than our wind tunnel outputs.

3.3 Annual Energy Production

We used power output results for our V2 generator, shown in Figure 35, as well as the average wind speed in Vallejo, CA of 3.9 m/s and the Rayleigh probability distribution for wind speeds to calculate our expected AEP of 39,835 Wh.

Chapter 4: Influence of Previous Design

Our previous years' designs and performance assisted in identifying key factors to maintain and improve upon creating a strong foundation for us to build upon. After determining these fundamental design decisions, each subteam (blades, mechanical, generator, instrumentation, controls & electrical, and foundation) virtually redesigned everything to ensure functionality through a simplistic and robust design.

Previous Designs	Influence on Current Design
Safety Task Accomplished by Feathering Blades	Created new, robust pitch system to ensure completeness of safety task
Custom Built Generator	Eliminates cogging torque, allowing for high power generation at lower wind speeds
Turbine State considerations for Mechanical Loading	Similar states with updated characteristics of current turbine assembly
Force Analysis of Full Turbine Assembly up to 22 m/s	Similar calculations with updated dimensions and characteristics of current turbine assembly.

Chapter 5: Commissioning Checklist

Before Installation into the wind tunnel and the commissioning begins, we will ensure that:

1) Nacelle is Built (Blades, Pitch, Generator, Linear Actuator Assembly connected and secured to the aluminum rail, which is connected to the stanchion and the upper tube), and Individual Parts have been inspected
2) Foundation has been installed and placed under the tunnel with the stub piece connected
3) Power and Signal Connection have been fed through foundation and stub piece

After these steps have been conducted and verified, commissioning will commence with all Installation Commissiong Tasks being conducted and/or verified by a team lead. Each Task will then be conducted and/or verified again by a different Team Lead.

Installation Commissioning Task	Certification #1	Certification #2
Inside of Tunnel Tasks		
Feed Power and Signal Cables through Tower		
Secure Turbine Tower to the stub piece		
Mount Nacelle to Tower		
Connect Power and Signal Cables to Nacelle		
Orient Rotor Axis In-line with Wind Direction		
Inspect Integrity of Blades (Cracks, Surface Inconsistencies, etc.)		
Verify Components are Secured to Frame (push/pull test)		
Ensure Expected Smooth Rotation of Rotor		
Visually Verify Proper Range and Operation of Pitch Assembly		
Outside of Tunnel Tasks		
Verify Power and Signal Cable Connections with Multimeter Continuity Test		
Connect Wall Power to Receptacle on Load Side Box and Close Switch		
Connect Power and Signal Cables to Turbine Side and Load Side Control Boxes and the PCC Respectively		
Connect E-Stop Out Wire to PCC Connection		
Verify All Sensors and Communication Devices Power Indication Lights		
Upload Manual Control Program		
Increase Windspeed to 5 m/s and Verify Proper Operation of Pitch System, Various Sensors, and Positive Power		
Upload Competition Turbine Testing program		

Bibliography

[1] "Blade Design Overview — QBlade Documentation 2.0.6.4 documentation." Available: https://docs.qblade.org/src/user/blade/blade.html.

[2] 3DXTech, "Technical Data Sheet: CarbonX™ CF-PLA 3D Printing Filament" Available: https://www.3dxtech.com/wp-content/uploads/2021/03/PLA_CF-TDS-v03.pdf.

[3] "spl10b.pdf | Unified Engineering I, II, III, & IV | Aeronautics and Astronautics," MIT *OpenCourseWare*. Available: https://ocw.mit.edu/courses/16-01-unified-engineering-i-ii-iii-iv-fall-2005-spring-2006/resources/spl10b/

[4] J. Nelson *et al*., " Cal Maritime Collegiate Wind Technical Design Report 2023," California State University Maritime Academy, 2023.

[5] M. Sessarego and D. Wood, "Multi-dimensional optimization of small wind turbine blades," Renewables, vol. 2, no. 1, p. 9, Dec. 2015, doi: 10.1186/s40807-015-0009-x. Available: https://jrenewables.springeropen.com/articles/10.1186/s40807-015-0009-x.

[6] Ragheb, M. "Optimal rotor tip speed ratio." Lecture notes of Course no. NPRE 475, 2014. Available: http://users.wpi.edu/~cfurlong/me3320/DProject/Ragheb_OptTipSpeedRatio2014.pdf.

[7] Rapiddirect, "Acetal vs Delrin: What Are Their Differences," rapiddirect. Accessed: Apr. 13, 2024. [Online]. Available: https://www.rapiddirect.com/blog/acetal-vs-delrin-what-are-their-differences/

[8] "Gorilla Epoxy," *Gorilla Glue*. Available: https://www.gorillatough.com/product/gorilla-epoxy/.

[9] "PolyLite™ PETG," Polymaker US. Accessed: Apr. 15, 2024. [Online]. Available: https://us.polymaker.com/products/polylite-petg.

[10] Actuonix Motion Devices, Inc, "Miniature Linear Motion Series · L12" 2019. Available: https://www.actuonix.com/assets/images/datasheets/ActuonixL12Datasheet.pdf.

[11] Melexis, "Hall Latch – High Sensitivity", US1881, January 2006. https://www.sparkfun.com/datasheets/Components/General/Hall-US1881EUA.pdf

[12] Sensirion, "Differential Pressure Sensor with Analog Output", SDP8xx-Analog, March 2018. https://sensirion.com/media/documents/68DF0025/6167E542/Sensirion_Differential_Pressure_Datasheet_SDP8xx_Analog.pdf

[13] Texas Instruments, "Ultra-Small, Low-Power, 16-Bit Analog-to-Digital Converter with Internal Reference", SBAS444B, May 2009, Revised October 2009. https://cdn-shop.adafruit.com/datasheets/ads1115.pdf

[14] Microchip, "12-Bit Digital-to-Analog Converter with EEPROM Memory in SOT-23-6", MCP4725, 2009. https://cdn-shop.adafruit.com/datasheets/mcp4725.pdf

[15] Texas Instruments, "INA228 85-V, 20-Bit, Ultra-Precise Power/Energy/Charge Monitor With I 2C Interface", SLYS012A, January 2021, Revised May 2022. https://www.ti.com/lit/ds/slys021a/slys021a.pdf?ts=1713330686996

[16] Texas Instruments, "ISO154x Low-Power Bidirectional I2C Isolators", SLLSEB6E, July 2012–Revised April 2019. https://cdn-learn.adafruit.com/assets/assets/000/099/320/original/iso1540.pdf?1612894897

[17] PJRC, "Teensy 4.1 Development Board", Revised March 2023. https://www.pjrc.com/store/teensy41.html